PNAS RESEARCH ARTICLE | DEVELOPMENTAL BIOLOGY
BIOPHYSICS AND COMPUTATIONAL BIOLOGY

The developmental mechanics of divergent buckling patterns in the chick gut

Hasreet K. Gill[a,1], Sifan Yin[b,1], John C. Lawlor[a], Tyler R. Huycke[a,c], Nandan L. Nerurkar[d], Clifford J. Tabin[a,2], and L. Mahadevan[b,e,f,2]

Affiliations are included on p. 11.

Edited by Marianne Bronner, California Institute of Technology, Pasadena, CA; received June 30, 2023; accepted May 6, 2024

Tissue buckling is an increasingly appreciated mode of morphogenesis in the embryo, but it is often unclear how geometric and material parameters are molecularly determined in native developmental contexts to generate diverse functional patterns. Here, we study the link between differential mechanical properties and the morphogenesis of distinct anteroposterior compartments in the intestinal tract—the esophagus, small intestine, and large intestine. These regions originate from a simple, common tube but adopt unique forms. Using measured data from the developing chick gut coupled with a minimal theory and simulations of differential growth, we investigate divergent lumen morphologies along the entire early gut and demonstrate that spatiotemporal geometries, moduli, and growth rates control the segment-specific patterns of mucosal buckling. Primary buckling into wrinkles, folds, and creases along the gut, as well as secondary buckling phenomena, including period-doubling in the foregut and multiscale creasing-wrinkling in the hindgut, are captured and well explained by mechanical models. This study advances our existing knowledge of how identity leads to form in these regions, laying the foundation for future work uncovering the relationship between molecules and mechanics in gut morphological regionalization.

gut | morphogenesis | modeling | mechanics

Significance

The esophagus, small intestine, and large intestine arise from a common early gut tube and adopt unique morphologies, but how the embryo differentially shapes gastrointestinal subregions has remained unclear. The inner epithelial surface is the site of critical digestive processes and, accordingly, develops region-specific wrinkled morphologies and cell type repertoires. Here, we combine physical measurements with theory and computations to determine the mechanical basis for positional differences in lumen folding along the embryonic chick gut. Our findings offer insight into basic intestinal development and the longstanding problem of how the embryo sculpts specialized forms from a common, initially uniform precursor.

The appearance of a regionalized gastrointestinal (GI) tract, comprising a foregut, midgut, and hindgut, likely dates to the ancestor of Cnidaria and Bilateria, over 600 million years ago (1). During early stages of development, a conserved molecular toolkit assigns anteroposterior (AP) identities along the primordial intestinal tract, which, in vertebrates, is a simple endodermal epithelial tube surrounded by the splanchnic lateral plate mesoderm (2). Expression of transcription factors, such as those encoded by Hox and ParaHox genes, along with polarized morphogen gradients along the AP axis (e.g., Shh, Bmp, and Wnt), demarcate regional boundaries in the endoderm and mesoderm beginning as early as gastrulation (2–4). As development progresses, subregions within each compartment adopt unique macroscale dimensions and specialized mucosal, or inner endodermal, surface morphologies that facilitate their functions.

The mature foregut-derived esophagus, midgut-derived small intestine, and hindgut-derived large intestine perform complementary roles in digestion that together ensure efficient processing of food. The epithelium is critical not only for secreting mucus and extracting water and nutrients but also for protection against pathogens and mechanical insults (5). The esophagus is the site of food intake into the GI tract, and across birds, mammals, and reptiles, it primarily develops broad "longitudinal" or "axial" ridges that are aligned along the gut long axis (Fig. 1 *A* and *B*) (6, 7). These ridges are thought to permit tube distension and accommodate a food bolus without rupture (8, 9). In humans and other mammals, "circumferential" folds oriented orthogonally to axial folds have only been reported in the context of esophageal disease—where axial folds also become reduced in depth and number—or as transient occurrences in healthy samples (10, 11). The epithelium of the esophagus in the mouse and human is initially pseudostratified and cuboidal and progressively thins to become a stratified squamous epithelium, which is renewed via proliferating progenitors in the basal layer (12).

In the small intestine, long, finger-like epithelial structures called villi are tightly packed and extend into the lumen to maximize surface area for nutrient absorption. Each villus has multiple associated crypts—invaginations that house intestinal stem cells (ISCs)—and along the crypt–villus axis, ISCs give rise to absorptive and secretory cell types with highly reproducible spatial organization (reviewed in refs. 13 and 14). The architecture of the small intestinal epithelium is thus crucially tied to its purpose.

Author contributions: H.K.G., S.Y., T.R.H., C.J.T., and L.M. designed research; H.K.G., S.Y., and J.C.L. performed research; S.Y., N.L.N., and T.R.H. contributed new reagents/analytic tools; H.K.G., S.Y., and J.C.L. analyzed data; and H.K.G., S.Y., C.J.T., and L.M. wrote the paper.

The authors declare no competing interest.

This article is a PNAS Direct Submission.

Copyright © 2024 the Author(s). Published by PNAS. This article is distributed under Creative Commons Attribution-NonCommercial-NoDerivatives License 4.0 (CC BY-NC-ND).

[1]H.K.G. and S.Y. contributed equally to this work.

[2]To whom correspondence may be addressed. Email: lmahadev@g.harvard.edu or tabin@genetics.med.harvard.edu.

This article contains supporting information online at https://www.pnas.org/lookup/suppl/doi:10.1073/pnas.2310992121/-/DCSupplemental.

Published July 5, 2024.

Downloaded from https://www.pnas.org by "HARVARD UNIVERSITY, CABOT SCIENCE LIBRARY" on August 11, 2024 from IP address 140.247.148.200.

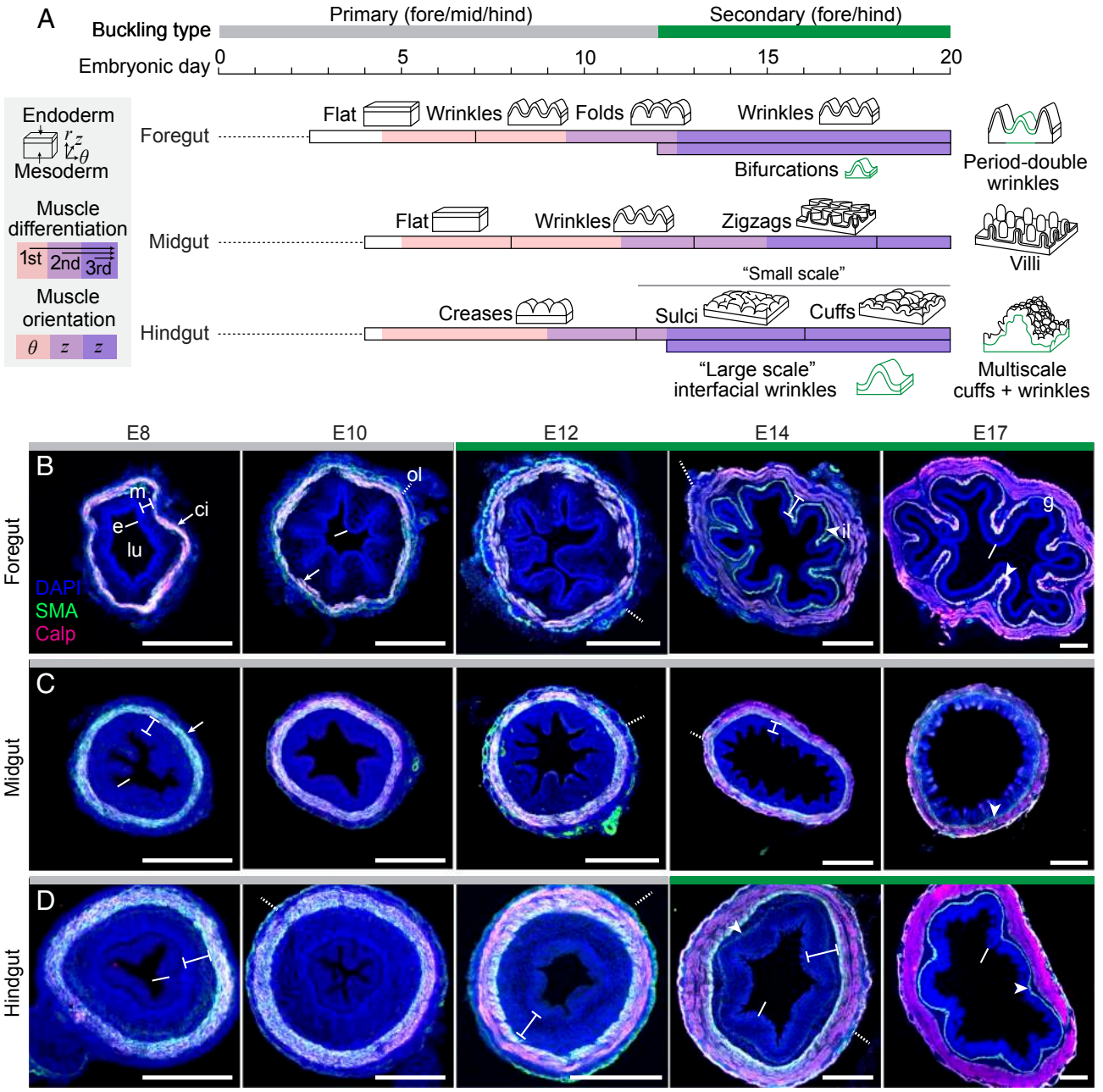


Fig. 1. Gut compartments develop distinct morphologies. (*A*) Timeline of lumen morphogenesis for each region (Foregut, Midgut, and Hindgut). Dashed lines, periods prior to tubulogenesis; boxes, folded states, with accompanying cartoons. Colored regions correspond to muscle layers present: pink, circumferential; light purple, circumferential and outer longitudinal; dark purple, circumferential, outer longitudinal, and inner longitudinal layers. Gray and green bars above the timeline highlight embryonic periods when primary and secondary buckling phenomena are present, respectively, and secondary components of folding pattern cartoons are colored in green. (*B–D*) Transverse sections over time in the (*B*) Foregut, (*C*) Midgut, and (*D*) Hindgut immunostained for nuclei (DAPI), early (SMA) and late (Calponin1) smooth muscle (m and brackets, mesenchyme; e and line, endoderm; lu, lumen; ci and arrow, circumferential muscle; ol and dashed line, outer longitudinal layer; il and arrowhead, inner longitudinal layer; gray and green bars, primary and secondary buckled forms, respectively). (Scale bar, 200 μm.)

The mucosal surface of the large intestine, or colon, is often reported to be like that of the small intestine (due to the presence of crypts and ISCs that renew the epithelium) but devoid of villi and thus "flat" (15, 16). However, many have noted the appearance of reticulated surface folds and/or structures analogous to villi—"colonic villi" or "cuffs"—in humans that sometimes disappear with distension (17–19). In addition, the colon exhibits a wide array of absorptive and secretory cell types, with some analogous to those of the small intestine (20, 21).

Despite our wealth of knowledge surrounding the molecular underpinnings of regional epithelial features, the morphogenetic processes that differentially shape regions along developing GI tract are still a mystery. In the chick midgut, villi form through primarily a mechanical process, where three sequentially forming smooth muscle layers drive stepwise, orthogonal buckling instabilities (22). The differentiation of a circumferentially aligned muscle layer within the gut mesoderm generates a region of undifferentiated subepithelial mesenchyme, constraining its growth and growth of the inner endoderm until they buckle into longitudinal (axial) wrinkles, which are marked by a uniformly sinusoidal shape, that extend along the length of the midgut (Fig. 1*A*). Then, a longitudinal muscle layer forms on the outer

Downloaded from https://www.pnas.org by "HARVARD UNIVERSITY, CABOT SCIENCE LIBRARY" on August 11, 2024 from IP address 140.247.148.200.

side of the circumferential layer, followed by another muscle layer on the inner (luminal) side. These muscle layers, hereafter referred to as "outer longitudinal" and "inner longitudinal," respectively, constrain growth in the orthogonal direction, leading to the buckling of axial ridges into sinusoidal zigzag wrinkles that become increasingly compressed and eventually form primordial villi, or "protovilli."

In each step, buckling occurs to ease residual stress from differential growth. Indeed, residual stresses from mismatched strains between growing layers fundamentally drive the formation of diverse buckled shapes in a variety of natural contexts (23, 24). Given that similar morphologies to the esophageal and large intestinal mucosal surfaces have been described using material and mathematical models, we reasoned that the variation in lumen morphology along the chick gut can be explained by regionally defined physical properties, which, in turn, lead to unique folding modes during constrained growth (25, 26). Furthermore, the conserved morphological features of the esophagus, small intestine, and large intestine (longitudinal wrinkles, villi, and disordered outgrowths), combined with their simple tubular geometry that allows for less computationally complex modeling, makes these regions particularly well-suited to this question of differential lumen shaping within the gut.

Results

Gut Compartments Adopt Distinct Epithelial Folding Patterns. To begin understanding how morphologies along the developing gut diverge, we first carefully characterized circumferential and axial buckling in each compartment over time using transverse and sagittal tissue sections. Early gut compartments each give rise to multiple intestinal structures beyond those we focus on in this study; however, for simplicity, we refer to the presumptive esophagus in the anterior foregut, presumptive small intestine in the central midgut, and presumptive large intestine in the anterior hindgut simply as "foregut," "midgut," and "hindgut," respectively. Consistent with our previous work and longstanding observations of chick gut development, the midgut lumen first forms longitudinal sinusoidal wrinkles (Fig. 1 *A* and *C*), which progressively decrease in wavelength before buckling orthogonally into zigzag sinusoidal wrinkles followed by zigzag folds (laterally self-contacting wrinkles), at day 14 of development (E14) (*SI Appendix*, Fig. S1 *A* and *B*). Zigzags are further compressed and undergo local rotations that pattern the positions of villi (22).

Early morphogenesis of the foregut is like that of the midgut: Modest longitudinal wrinkles appear in the endoderm–mesenchyme composite around E8; these progress into laterally self-contacting axial folds by E10 and wrinkles again at E12 that are broader and fewer in number than those of the midgut at the same stage (Fig. 1 *A* and *B* and *SI Appendix*, Fig. S1 *A* and *B*). Subsequent elaboration of midgut wrinkles by E17 contrasts with the relatively steady number of consistently wider wrinkles in the foregut (*SI Appendix*, Fig. S1 *C* and *D*). The pattern wavelengths of the foregut and midgut are initially similar, but as the midgut develops zigzags and protovilli from E14 onward, the foregut progressively grows in circumference, resulting in significantly greater distances between wrinkle peaks (*SI Appendix*, Fig. S1*E*). The most striking distinction from the midgut, however, is that longitudinal wrinkles are maintained until late stages in the foregut without undergoing an additional form of circumferential (orthogonal) buckling as with zigzags (Fig. 1*B* and *SI Appendix*, Fig. S1 *A* and *B*).

While the midgut and foregut first form smooth wrinkles comprising both the endoderm and mesenchyme layers, the hindgut forms creases, or superficial, fold-like structures that exist only on the surface of the endoderm (Fig. 1*D* and *SI Appendix*, Fig. S3*A*). Creases are initially longitudinal but eventually form branched sulcal patterns between E12 and E14, still just on the surface of the endoderm (Fig. 1*D* and *SI Appendix*, Fig. S1*A*) (27). Creased sulci then gradually give way to smooth wrinkling of the endoderm–mesenchyme composite to form short and wide cuffs by E17, which are superficially similar in appearance to villi, but distinct in their geometry and spatial arrangement on the lumen surface (Fig. 1*D* and *SI Appendix*, Figs. S1*A* and S3*A*) (27). Notably, although the hindgut does form intermediate morphologies—longitudinal creases and sulci—they do not appear to prefigure subsequent patterns as in the midgut, where each ridge buckles into a zigzag, followed by each zigzag arm bulging to initiate the formation of a villus (22). Thus, the midgut, foregut, and hindgut share some aspects of lumen morphogenesis (orientation of primary buckling, as defined in the next section, and timing of folding transitions) but ultimately adopt distinct trajectories to achieve region-specific epithelial structures (Fig. 1*A*).

Foregut and Hindgut Lumens Develop Secondary Buckling Patterns. After the early formation of longitudinal wrinkling/folding and creasing in the foregut and hindgut, respectively, these regions then develop and maintain two-dimensional hierarchical folding patterns that are ultimately absent in the midgut, where symmetric and uniform villi tile a flat cylindrical surface (Fig. 1 *A* and *C*). In the foregut, following the initial appearance of a symmetrical buckling pattern at E10, some folds spontaneously form bifurcations at their bases, which are maintained as wrinkles reappear and scale with tube growth from E12 onward. (Fig. 1 *A* and *B*, green bar, *SI Appendix*, S1*B*, *C* and *E*). As a result, foregut wrinkles ultimately display a period-doubling phenomenon, where large and small amplitude waves alternate (Fig. 1*A*). Though these wrinkles also appear transiently during early stages of midgut ridge formation and growth, they are eventually lost when the lumen buckles into zigzags.

In the hindgut, we see a distinct and intriguing phenomenon where, coincident with the formation of sulci around E14, broad, radially symmetric longitudinal buckling appears at the endoderm–mesenchyme interface (Fig. 1*D*). While these initially resemble self-contacting folds, they grow to form wrinkles that increase in number with radial growth and are even maintained when surface creases are replaced with smoothly wrinkled cuffs (Fig. 1*D* and *SI Appendix*, Fig. S3*A*). The hindgut therefore develops a multiscale pattern on two length scales concurrently—"small-scale" cuffs with "large-scale" interfacial wrinkles (Fig. 1*A*).

Though both period-doubling in the foregut and small/large-scale buckling in the hindgut are multiscale patterns which, by definition, exhibit two or more characteristic wavelengths, for simplicity we use "multiscale" only in reference to the hindgut morphology. In addition, we refer to the initial states of foregut uniform amplitude wrinkling and hindgut creasing as "primary" buckling patterns, and subsequent foregut period-doubling and hindgut multiscale buckling as "secondary" buckling or "postbuckling" patterns. These correspond to the first and second growth-induced mechanical bifurcations in each region, respectively, with the latter appearing as external loading (compression/growth) increases (Fig. 1*A*, gray and green bars). Because both of these architectures involve the simultaneous

Downloaded from https://www.pnas.org by "HARVARD UNIVERSITY, CABOT SCIENCE LIBRARY" on August 11, 2024 from IP address 140.247.148.200.

superposition of two buckling motifs (large and small amplitude wrinkles in the foregut and large-scale wrinkles with and small-scale creases or cuffs in the hindgut), we consider them to be distinct from the wrinkle-to-zigzag transition in the midgut, where longitudinal wrinkles are lost upon zigzag formation. Differences between compartmental forms therefore extend to postbuckling events that contribute to morphological and likely functional specialization of the hindgut and foregut.

Differences in Smooth Muscle Constraints Do Not Explain Morphological Differences. Given that stepwise lumen folding in the small intestine depends on sequential differentiation of three muscle layers, we began by asking whether differences in muscle constraints explain deviations from the midgut buckling program elsewhere in the gut. We therefore observed smooth muscle stained with early (smooth muscle actin, SMA) and late (calponin 1) markers in foregut, midgut, and hindgut sections, as well as muscle orientations in stained whole-mount samples (Fig. 1 *B*–*D* and *SI Appendix*, Fig. S2 *A* and *B*). We first found that all regions formed circumferential, outer longitudinal, and inner longitudinal muscle layers in succession, though each layer differentiated slightly earlier in the foregut and hindgut than in the midgut (Fig. 1*A*). Focusing on properties of the first two muscle layers to form (circumferential and outer longitudinal) which drive the critical ridge and zigzag buckling events in the midgut, we concluded that layer fiber orientations, placements, and maturation timelines are essentially identical between regions (Fig. 1 *B*–*D* and *SI Appendix*, Fig. S2 *A* and *B*).

It was not until we considered the third, inner longitudinal layer, that we saw differences in muscle properties between regions. While it lies flat and closely adjacent to the circumferential muscle in the midgut, this layer differentiates deep within all wrinkles in the foregut, and large-scale wrinkles in the hindgut, and therefore achieves a wrinkled shape (Fig. 1 *B* and *D*). SMA fibers within this layer are still clearly oriented along the longitudinal axis in the foregut and hindgut, but some intermixed fibers with random orientations are also present (*SI Appendix*, Fig. S2 *A* and *B*). However, though these differences in the muscularis mucosa may be relevant to later properties of mucosal folds, they arise after the lumens adopt distinctive features (Fig. 1*A*). Though it is still possible that regional variation in smooth muscle thickness and stiffness affects lumen buckling along the gut, we cannot fully explain morphologies from differences in the first two muscle layers alone.

The Ratio of Endoderm to Mesenchyme Thickness Increases and Radius Decreases from the Foregut to Hindgut. We next considered whether variations in relative geometric and mechanical properties of the constrained inner layers cause regions to assume unique configurations as they alleviate residual stress. To estimate radial growth over time, we used transverse sections to measure endoderm and mesenchyme thicknesses, as well as inner and outer tube radii (Fig. 2*A*). Though these measurements are taken from samples in their deformed (not stress-free) states, they nonetheless allow us to identify region-specific patterns in geometric changes over time. Inner radius is the distance from the center of the lumen to the apical edge of the endoderm, and outer radius is the distance from the center of the lumen to the inner edge of the circumferential muscle layer (Fig. 2*A*). We then determined the ratio of endoderm to mesenchyme thickness and inner to outer radius, which are hereafter referred to as "thickness ratio" and "radius ratio," respectively.

Though we collected these parameters during the entire time frame relevant to lumen morphogenesis (E8 to E18), we first focused on the period when primary buckling patterns appear, from E8 to E12. Later-stage data (E12 to E18) from all three regions were then used to investigate the appearance of secondary buckling patterns in the hindgut and foregut, as discussed later. Also, to compare against the existing model of midgut morphogenesis, we mainly considered differences in the foregut and hindgut relative to the midgut, though other pairwise comparisons are noted below as well.

We first noted that all three regions show a decrease in thickness ratio over time during primary buckling (Fig. 2*D*, gray bar along x-axis), generally due to the combination of a net decrease in endoderm thickness and increase in mesenchyme thickness (Fig. 2*B*). During E8 to E12 in the hindgut, a substantially thicker endoderm results in a higher thickness ratio than in the midgut across stages and in the foregut after E8 (Fig. 2 *B* and *D*). By contrast, in the foregut, a steeper rate of mesenchymal thickening than in the midgut between E8 and E12 (Fig. 2*B*, compare curve slopes) effectively leads to a more dramatic decrease in the relative thickness of the endoderm (thickness ratio) (Fig. 2 *B* and *D*). For tube radii during primary buckling, the midgut and foregut show proportional increases in inner and outer radii, but both the inner radius (lumen size) and outer radius are larger in the foregut than in the midgut from E8 to E12 (Fig. 2 *C* and *E*). By contrast, the lumen remains small in the hindgut, and the outer radius is as large as that of the foregut (Fig. 2*C*).

Thus, from E8 to E12, the foregut and hindgut grow more radially than the midgut through region-specific phenomena—namely, increase in lumen size in the foregut and tube wall thickening in the hindgut (Fig. 2 *B* and *C*). Furthermore, in the midgut and hindgut, proportional changes in endoderm and mesenchyme thickness from E8 to E10 contrast with the anisotropic layer growth indicated by relative thinning of the endoderm in the foregut (compare slopes of E8 to E10 thickness ratios in Fig. 2*D*). Together, these simple measurements capture differences in radial growth between regions when primary buckling patterns emerge, which we expect reflect and influence how the tissues respond to mechanical constraint.

The Ratio of Endoderm to Mesenchyme Modulus Decreases from Anterior to Posterior in the Gut. Differences in relative stiffness affect how force is translated into deformation in a material, so to further understand variations in endodermal buckling along the gut, we determined its modulus relative to that of its substrate, the mesenchyme, in each region. To measure Young's modulus, we used fine dissections to carefully separate the endoderm and endoderm–mesenchyme composite from the circumferential and outer longitudinal muscle layers, and then applied a custom mesomechanical testing setup in which a fine tungsten cantilever is used as a force transducer (Fig. 2*F* and *Materials and Methods*) (22, 28, 29).

While endoderm modulus was measured directly, modulus of the mesenchyme (a loose collection of cells suspended in extracellular matrix) was extracted from composite properties of the endoderm and mesenchyme, approximating the two as a bilayered composite loaded in parallel (*SI Appendix*, Fig. S4 *A* and *B*). Our measurements at E10 revealed a striking trend in endoderm and mesenchyme moduli along the rostrocaudal axis. The endoderm is stiffest in the foregut and softest in the hindgut, while the mesenchyme is softest in the foregut and stiffest in the hindgut (Fig. 2*G* and *SI Appendix*, Fig. S4*C*). The

Downloaded from https://www.pnas.org by "HARVARD UNIVERSITY, CABOT SCIENCE LIBRARY" on August 11, 2024 from IP address 140.247.148.200.

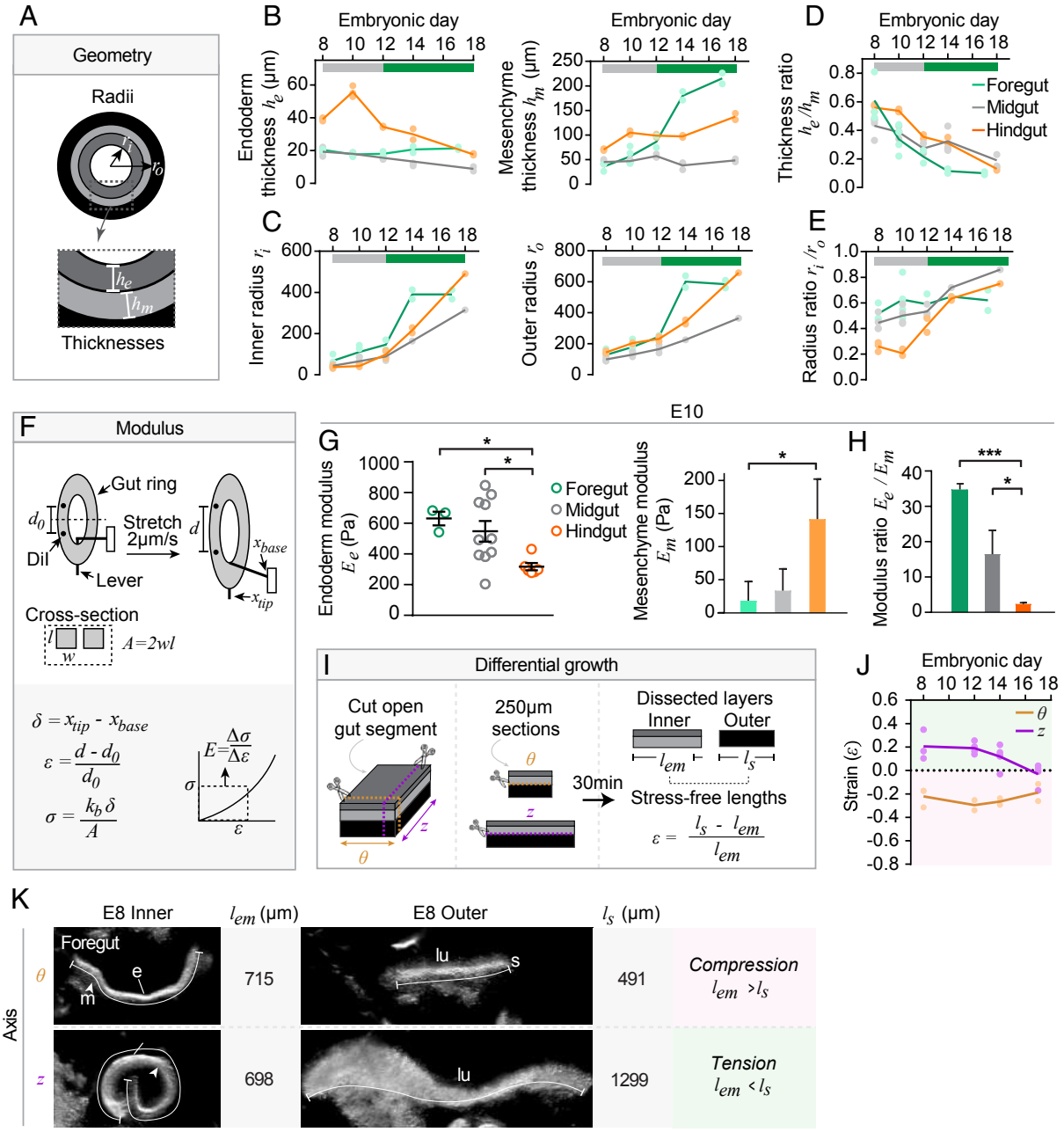


Fig. 2. Geometric and mechanical properties along the developing gut. (*A*) Schematic illustration of radial geometric measurements collected from transverse sections. Black, muscle; light gray, mesenchyme (m); medium gray, endoderm (e). h, thickness; ri, inner radius; and ro, outer radius. (*B*) Endoderm and mesenchyme thicknesses and (*C*) inner and outer radii over time (n = 2 to 3 biological replicates each for parts *B* and *C*). (*D*) Ratios of inner endoderm-to-mesenchyme layer thicknesses, and (*E*) inner to outer radii for each region over time, determined from measurements in parts (*B* and *C*). Green and gray bars in parts (*B*–*E*) indicate time periods corresponding to the appearance of primary (in all three regions) and secondary (in the foregut and hindgut) buckling instabilities, respectively, as in Fig. 1*A*. (*F*) Method of modulus ratio measurement using uniaxial tensile testing. Above, top and side views of testing set up; below, measurements taken at the test start and at each time step, with calculations. (*G*) Endoderm (n = 3 to 10 gut segments from 2 to 3 biological replicates per condition) and mesenchyme modulus values at E10, and (*H*) ratios of endoderm to mesenchyme modulus. Error bars, SEM (see *SI Appendix*, Fig. S4*C* for individual composite modulus measurements). Statistical tests: One-way ANOVA with Tukey's MCT (*$P < 0.05$; ***$P < 0.001$). (*I*) Method of differential growth measurement. (*J*) Strain over time, green indicates tensile regime and pink is compressive (n = 3 biological replicates per axis). (*K*) Representative dissecting microscope images and measurements from E8. Tissue length (l) values in μm correspond to bracketed lines in images (e, endoderm; m and arrowhead, mesenchyme; s, muscle; and lu, lumen side).

endoderm-to-mesenchyme modulus ratio, therefore, decreases from 35 to 2 from the foregut to the hindgut (Fig. 2*H*).

In summary, during the appearance of distinct primary buckling instabilities in the chick gut from E8 to E12, the lumen and outer boundary of the foregut tube grow over time as a stiff endoderm layer grows against a soft mesenchyme; thickening of the mesenchyme progressively lowers the relative contribution of the endoderm to composite thickness. In the midgut, the endoderm is still stiffer than the mesenchyme, but layer thicknesses show minimal changes as the lumen and outer radius grow from E8 to E12. Finally, all tissues are thicker during this time in the hindgut, where a uniformly stiff endoderm–mesenchyme composite leads to a thick tube wall without growth of the lumen until after E10. These results suggest the presence

Downloaded from https://www.pnas.org by "HARVARD UNIVERSITY, CABOT SCIENCE LIBRARY" on August 11, 2024 from IP address 140.247.148.200.

of monotonic trends in material properties, relative radii, and relative tissue thicknesses along the gut long axis (*SI Appendix*, Fig. S4*C*).

Development of a Computational Model to Capture Buckling Patterns. Our measurements provide an overview of the mechanical and growth-related features associated with each region, but is this information sufficient to explain the appearance of distinct primary lumen patterns along the gut? Each morphological outcome depends on the complex interaction of multiple parameters, and the specific contribution of each property is extremely difficult to resolve experimentally. Therefore, systematically testing whether mechanical differences fully explain region-specific morphologies required turning to mathematical modeling.

The observed time-dependent evolution of thickness and radius ratios suggests a differential growth-induced mechanical instability as the mechanism for divergent lumen pattern formation. We therefore modeled the gut as a growing two-layer tube composed of endoderm and mesenchyme layers, as shown in Fig. 2*A*, which are constrained by the circumferential and outer longitudinal muscle layers. For simplicity, we focused on the cross-sectional patterns and considered a plane-strain 2D model (Fig. 3*A*). Also, because buckling of the midgut lumen has already received considerable attention, we mainly focused on the foregut and hindgut.

Based on the well-established theory of differential growth, the deformation gradient of tissues is multiplicatively decomposed to an elastic part and a growth part as $\mathbf{F} = \mathbf{A}\cdot\mathbf{G}$. The elastic tissue is modeled as neo-Hookean material with a volumetric strain energy density $W_{\mathrm{A}} = \frac{\mu}{2}\left[J_A^{-\frac{2}{3}}\mathrm{Tr}(\mathbf{A}\cdot\mathbf{A}^{\mathrm{T}}) - 3\right] + \frac{K}{2}(J-1)^2$, where $J_{\mathrm{A}} = \det\mathbf{A}$, μ is the elastic shear modulus and the bulk modulus $K = 10^3\mu$ makes the tissues almost incompressible. Spatiotemporal radial (r), circumferential (θ), and axial (z) growth ratios were fitted to measurements and incorporated to the growth tensor ($\mathbf{G}$) for both the endoderm and mesenchyme as $\mathbf{G} = \mathrm{diag}(g_r, g_\theta, g_z)$ (Fig. 3*A* and *SI Appendix*, Text).

For 2D models, longitudinal growth vanished $g_z = 1$, and radial and circumferential growth are estimated as $g_{r\alpha} = \bar{h}_\alpha/\bar{h}_{\alpha 0}$ and $g_{\theta\alpha} = \bar{r}_\alpha/\bar{r}_{\alpha 0}$ with $\alpha =$ "e" and "m" representing the endoderm and mesenchyme, respectively; the subscript "0" represents quantities at the initial configuration (Fig. 3*A*). Thickness and radius values used in these calculations are rescaled by the radius of the muscle layer r_o as $\bar{h}_\alpha = h_\alpha/r_o$ and $\bar{r}_\alpha = r_\alpha/r_o$. Using this differential growth model framework, we next used a series of simulations to computationally predict how the spatiotemporal geometric and mechanical parameters (i.e., the thickness and stiffness of endodermal and mesenchymal layers) can lead to divergent lumen morphologies.

Relative Endodermal Thinning Drives Primary and Secondary Wrinkling in the Foregut. Simulating foregut and hindgut morphogenesis required incorporating measured radii and thickness data into the model, but because our measurements from transverse sections represent stressed configurations, we first estimated the stress-free configuration at each time point using radial geometric parameters at the following time point. For instance, we used the stress-released geometry of E8 as the initial state for E10. Our model therefore considers dynamic changes in tube geometry over time using measured data.

At E8 in the foregut, we assumed an isotropic growth profile ($g_r = g_\theta$), and the initial geometry and modulus ratio were estimated from measurements. The resulting simulation mimics a smooth wrinkling pattern in the endoderm, consistent with the primary wrinkling pattern of the E8 foregut (Fig. 3*B* and Movie S1). Analogous longitudinal wrinkling was characterized computationally in the context of midgut morphogenesis (22), confirming the similarity and robustness of anterior gut morphogenesis before morphologies diverge. However, our simulations using isotropic growth were not able to recapitulate the self-contacting folds of the E10 foregut (Fig. 1*A*), indicating a need to refine the parameters of the foregut model and a divergence from that of the midgut.

As described above, thickness measurements in the foregut revealed a sharp decrease in the thickness ratio between the endoderm and mesenchyme from E8 to E12 (Fig. 2*D*). We therefore hypothesized that this observed relative thinning of the foregut endoderm may be relevant to specialization of the foregut primary buckling pattern from wrinkles to folds, and could be incorporated accordingly in our computational model. To both test this possibility and explore the parameter space, we designed two additional anisotropic growth profiles: endoderm thinning with or without mesenchyme thickening, similar to experimental observations of the foregut, and endoderm thickening (*SI Appendix*, Text). Simulations were then performed using each of these growth profiles instead of isotropic growth.

Interestingly, our results showed that we can only recapitulate the surface buckling of foregut at E10 if we introduce endodermal thinning into the radial growth profile (Fig. 3*B* and Movie S1). Importantly, the observed high endoderm-to-mesenchyme modulus ratio (Fig. 2*H*) is also necessary to replicate foregut folding in the model. This pattern begins as smooth sinusoidal wrinkling, and with radial compression of the mesenchyme, the peaks and valleys of the wrinkles widen and flatten, respectively (Figs. 1*A* and 3*B* and Movie S1). Eventually, the valleys are compressed until adjacent folds contact one another, forming a symmetry-breaking folding pattern like that of the foregut at E10 (Fig. 1 *A* and *B*). We concluded from these tests that simulating the shift in foregut primary buckling from wrinkling to folding requires incorporating endodermal thinning.

Next, we considered whether our computational framework could predict secondary buckling in the foregut. As mentioned, from E12 to E17, a novel period-doubling pattern emerges in the foregut lumen (Fig. 1 *A* and *B*). During this time, measurements indicate that relative thinning of the endoderm (i.e., a decrease in thickness ratio) continues as foregut mesenchyme thickness increases drastically (Fig. 2*B*). Inner and outer radii also increase more steeply than in other gut compartments from E12 to E14 (Fig. 2*C*), when the secondary morphology first begins to appear (Fig. 1*B*). To systematically investigate the mechanical and geometric drivers behind the emergence and stabilization of the period-double pattern, we first set the initial geometry and modulus ratio as measured at these time points in the foregut (*SI Appendix*, Table S1) and again performed test simulations by altering growth profiles to represent endoderm isotropic growth, thinning, and thickening. Fig. 3*C* shows three distinct postbuckling patterns due to isotropic and anisotropic (endoderm thickening and thinning) growth profiles. We first see that primary buckling into sinusoidal wrinkles is similar between the three cases. However, a progressive increase in the thickness of the endoderm ($g_r > 1$) relative to its radius (g_θ) can sustain symmetric wrinkles and leads to a pattern where the wrinkle peaks and valleys have almost the same thicknesses (Fig. 3*C*, blue curve). Endoderm isotropic growth ($g_r = g_\theta$), by contrast, can only partially inhibit the tendency for neighboring wrinkles to merge and forms rough period-doubles, as is sometimes

Downloaded from https://www.pnas.org by "HARVARD UNIVERSITY, CABOT SCIENCE LIBRARY" on August 11, 2024 from IP address 140.247.148.200.

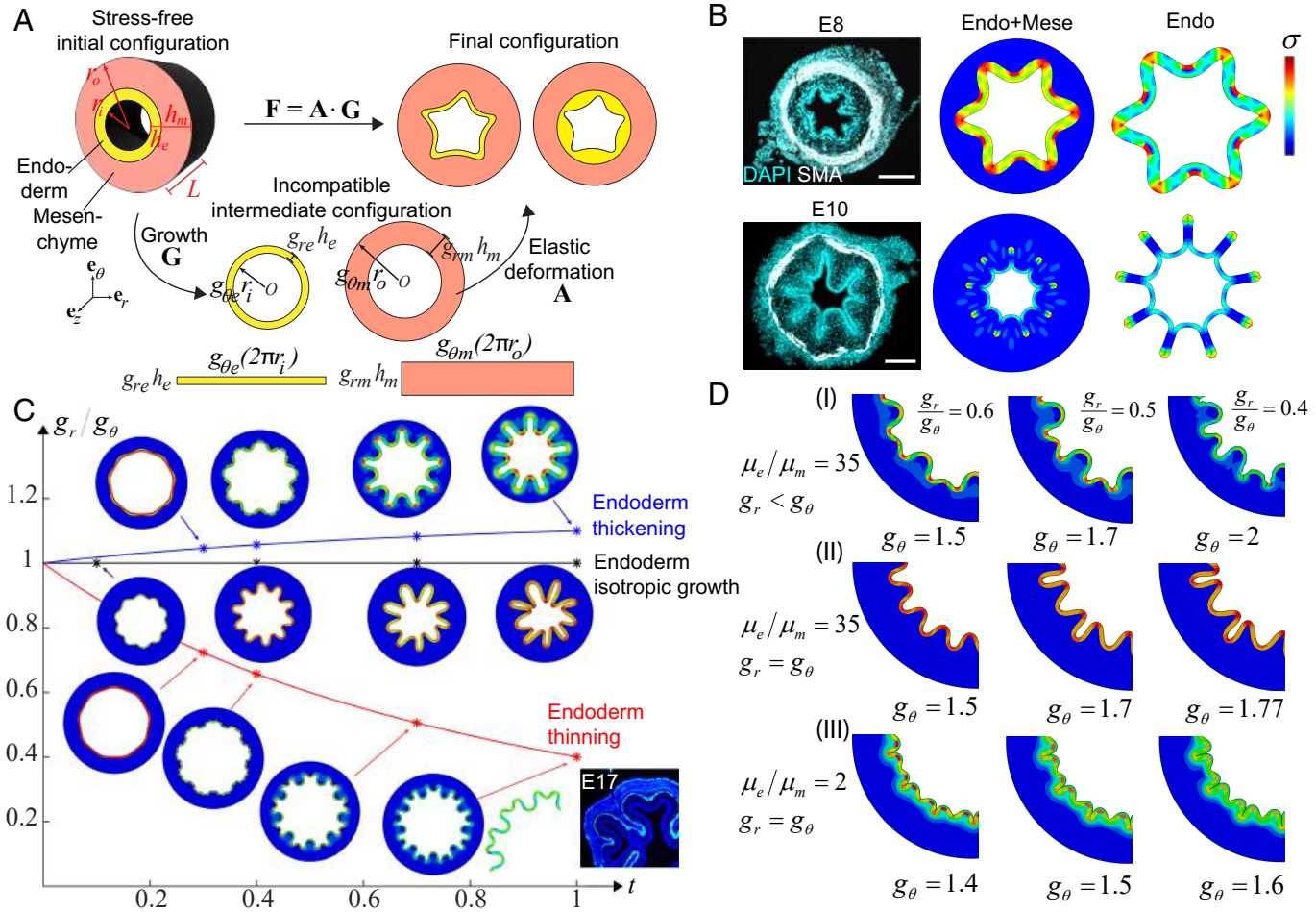


Fig. 3. Numerical model of gut lumen wrinkling and foregut results. (*A*) Schematic of numerical model and the steps of multiplicative decomposition of the deformation gradient F to simulate gut lumen buckling. (*B*) Primary wrinkling (E8, *Upper* row) and folding (E10, *Lower* row) of the foregut in early stages. Initial geometry at E8 is $r_i/r_o = 0.6$, $h_e/h_m = 0.3$, and the endoderm grows isotropically. Initial geometry at E10 is $r_i/r_o = 0.65$, $h_e/h_m = 0.2$, and the endoderm thins over the course of the simulation. (Scale bar, 100 μm.) (*C*) Growth models for period-doubling in the foregut. Endoderm thickening ($g_r = 1 + 1.2t$, $g_\theta = 1 + t$), isotropic growth($g_r = g_\theta = 1 + t$), and thinning ($g_r = 1 - 0.2t$, $g_\theta = 1 + t$) are computed. The endoderm thinning model (red line) captures the period-doubling in E17 foregut, shown in the *Inset*. The initial geometry at E17 is $r_i/r_o = 0.65$, $h_e/h_m = 0.2$. (*D*) Three typical period-doubling patterns modeled by endoderm thinning (*I*) and isotropic growth (*II* and *III*). Color indicates magnitude of stress.

seen in the prezigzag midgut (Fig. 3*C*, black curve) (22). Thus, growth profiles where the relative endoderm thickness is maintained or increases do not generate robust period-double wrinkles.

Much like self-contacting folds at E10, the remarkable feature of period-doubling at E17, where each wrinkle valley is split into two halves and wrinkles have alternating high and low amplitudes, can only be captured by implementing relative thinning of the endoderm ($g_r/g_\theta < 1$) (Fig. 3*C*, red curve). Amplifying endodermal thinning by increasing the mismatch between radial and circumferential growth rates leads to more dramatic period doubling with self-contacting folding (Fig. 3 *D*, *I* and Movie S3). Finally, to further understand the range of parameters that can generate these patterns, we also simulated foregut endoderm isotropic growth with varied geometries and modulus ratios. Under high, isotropic radial growth, we found that sinusoidal wrinkles can also adopt a pattern resembling period-doubling, where some valleys widen while adjacent valleys narrow (Fig. 3 *D*, *II* and Movie S3). However, the effect is less pronounced and the feature of alternating high and low amplitude waves is not achieved. Therefore, clearly alternating amplitudes in the period-double pattern depend both on endodermal thinning and sufficiently high growth rates.

Importantly, as with E8 and E10 simulations, our late-stage (E12 to E17) tests employ a high endoderm-to-mesenchyme modulus ratio to recapitulate foregut patterns, consistent with measured data (Fig. 2*H*). When we simulated folding using a low modulus ratio in the context of isotropic endodermal growth, wrinkles evolve to creases where every pair of adjacent peaks is squeezed and the valleys touch their neighbors to form "cusps" (Fig. 3 *D*, *III* and Movie S3). Cusps are like self-contacting folds, but the self-contact only occurs on the endoderm surface, while the endoderm–mesenchyme boundary remains flat or wrinkled. This is consistent with a known requirement for a high modulus ratio in smooth wrinkling instead of cusped creasing (25). Our model results indicate that the main feature regulating the transition from primary buckling to secondary postbuckling patterns in the foregut is decreasing relative thickness of its endoderm layer in the context of a high endoderm-to-mesenchyme modulus ratio.

Foregut Inner Layers Experience Axial Prestretch. Computational models thus far can explain morphological differences between the foregut and midgut by considering growth only along the circumferential and radial axes. However, an additional form of pattern differentiation between regions relies on the

Downloaded from https://www.pnas.org by "HARVARD UNIVERSITY, CABOT SCIENCE LIBRARY" on August 11, 2024 from IP address 140.247.148.200.

appearance of axial compression. Axial constraint causes inner layers in the midgut to buckle from ridges into zigzags, and, as we describe elsewhere, contributes to sulci formation in the hindgut (27). But, since the foregut develops the same three muscle layers as the midgut (Fig. 1 *B* and *C*), why does it maintain ridges instead of forming zigzags?

To address this issue, we first considered whether the magnitude of axial compression is different between the midgut and foregut. To measure differential growth, we used fine dissections to separate the inner composite from muscle as with tensile testing, but now on both the circumferential and longitudinal axes (Fig. 2*I*). After allowing tissues to relax to their stress-free states, we measured strain as the percent change in length from the unstressed to stressed configurations.

In the midgut, circumferential compression appears prior to E8 and is maintained throughout morphogenesis, but longitudinal compression does not appear until longitudinal muscle differentiates at E12 (22, 27). In the foregut, circumferential compression appears as in the midgut—as shown for E8, the stress-free length of the inner composite is greater than that of the muscle that constrains its growth in the stressed configuration (Fig. 2 *J* and *K*). However, longitudinal strain is in the tensile regime for the entirety of lumen morphogenesis: For example, at E8, the dissected inner composite is shorter than muscle on the longitudinal axis (Fig. 2*K*). This means that the inner composite experiences sustained longitudinal prestretch, which is consistent with resistance to buckling on that axis. As a result, despite the presence of longitudinal muscle, zigzags fail to form in the foregut because inner layers are stretched longitudinally and are thus unable to deform.

Early Hindgut Creasing Patterns Are Consistent with Geometric and Material Properties. To test how mechanical parameters affect hindgut morphogenesis, we next turned our attention to the primary and secondary buckling patterns that emerge between E8 and E12 and after E12, respectively. Once again, we focus solely on the radial and circumferential axes in 2D, though the hindgut develops biaxial sulci from E12 onward (27).

Before E12, the hindgut forms a creasing pattern with progressively increasing crease number just on the surface of the endoderm (Fig. 1*D*). To simulate this primary lumen surface instability, we began by applying an isotropic growth model based on the observed coordinated and proportional radial growth of the endoderm and mesenchyme from E8 to E10 (Fig. 2 *B* and *D*), and incorporated the geometry and low modulus ratio of the early hindgut. As expected from previous work in flat bilayers and curved surfaces (25, 30), our model recapitulated the cusped surface patterns observed at these stages. Furthermore, we observe a trend of increasing cusp number as in the growing embryonic hindgut, where the simulated E8 lumen forms 3 cusps while the E10 hindgut forms 5, as a consequence of their unique tube geometries (Figs. 4*A* and 1*D* and Movies S4 and S5).

Multiscale Hindgut Buckling Requires Stabilization of Inner Creases. After E12 in the hindgut, as the endoderm thins (Fig. 2*B*) and the wavelength of creases decreases, a secondary buckling phenomenon emerges: multiscale buckling made up of small-scale surface creases with large-scale interfacial wrinkling. It is important to note that multiscale wrinkling appears simultaneously with the differentiation of the inner longitudinal muscle layer within the subepithelial mesenchyme (Figs. 1*D* and 4*D*). As we never observed wrinkling without inner longitudinal muscle, we are not yet able to conclude whether the instability precedes or follows muscle differentiation. However, given known contributions of smooth muscle to tissue mechanical properties, such as stiffness, it is likely that the unique placement and appearance of the inner longitudinal muscle in the hindgut affects buckling when it appears.

We began our investigation of secondary buckling in the hindgut by applying our growth model as before with varying geometric properties shown in Fig. 2 *B* and *E*, E12 to E18 (*SI Appendix*, Table S1); however, it was not possible to capture both creases and large-scale wrinkles simultaneously, as creases tended to disappear with the onset of secondary buckling. One possible explanation for this finding is that the hindgut relieves its residual stress through a yet-unknown form of tissue remodeling

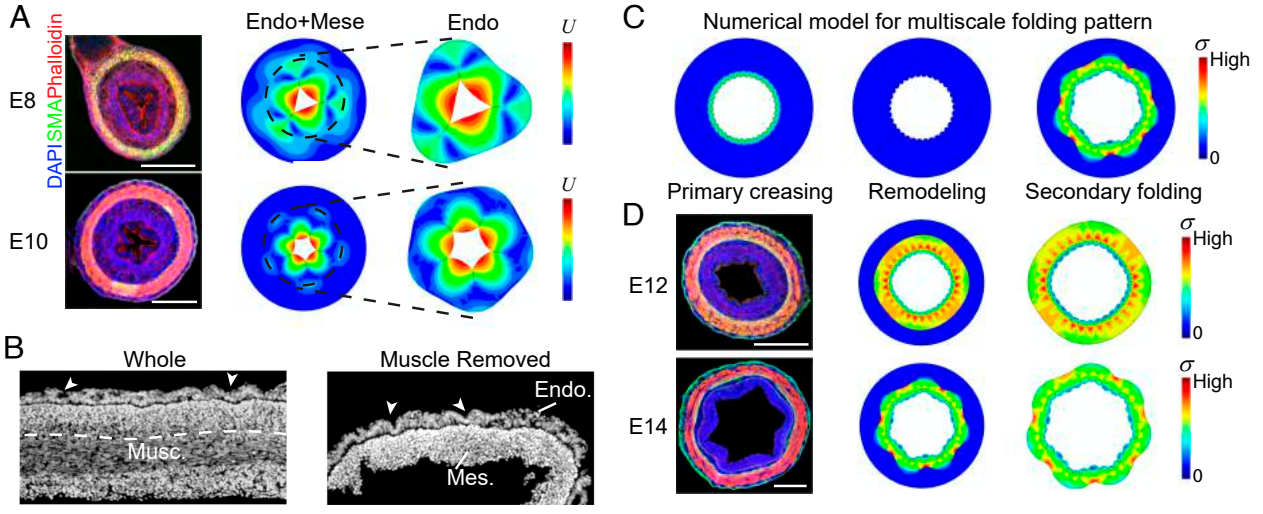


Fig. 4. Simulation models for hindgut primary creasing and secondary folding. (*A*) Experimental and simulated primary creasing patterns of hindgut at E8 and E10. (*B*) Sagittal view of creasing patterns of the E12 hindgut (DAPI). *Left*, all three layers; *Right*, endoderm and mesenchyme layers with muscle dissected away. Dashed line, boundary between the inner longitudinal muscle layer and endoderm and mesenchyme layers. Arrowheads indicate prior and persistent creases on the endoderm surface (Endo., endoderm; Mes., mesenchyme; and Musc., muscle). (*C*) Numerical model for multiscale pattern formation showing three phases that progress from a bilayer initial configuration: primary creasing, remodeling-induced stress release, and secondary wrinkling of the new endoderm layer with increasing thickness and modulus. Color indicates magnitude of mises stress. (*D*) Stained sections and simulations showing multiscale creasing and folding of hindgut at E12 and E14. (Scale bar, 200 μm.)

Downloaded from https://www.pnas.org by "HARVARD UNIVERSITY, CABOT SCIENCE LIBRARY" on August 11, 2024 from IP address 140.247.148.200.

prior to the appearance of interfacial (large-scale) wrinkling. To test this hypothesis, we dissected the outer circumferential muscle boundary away from the inner endoderm–mesenchyme composite to determine whether creases resolve into a flat surface when residual stress is removed (Fig. 4*B*). Remarkably, we found that creases are maintained, indicating that surface epithelial cells stabilize their configuration, possibly through downstream cell-biological phenomena such as cytoskeletal remodeling, or that the endoderm is instead constrained by the mesenchyme layer (27). In either case, we expect that the primary creasing pattern would be unaffected by secondary folding due to growth against outer muscle.

To determine whether the persistence of creases after circumferential muscle removal can explain coincident small and large-scale morphologies in the hindgut, we developed a three-step growth profile (Fig. 4*C*). First, the innermost endoderm layer experiences isotropic growth with a low modulus ratio (Fig. 2*H*), as established above for primary buckling, $\mu_e/\mu_m = 2$ (Fig. 2*H*). After this point, residual stress in the endoderm is released and the inner longitudinal smooth muscle layer differentiates. For simplicity and because we anticipate a role for this layer in multiscale buckling, in subsequent steps of the simulation, the true endoderm and subepithelial layer are combined and considered to be one "endoderm" layer. Later stage modulus measurements indicate an increase in both endoderm and mesenchyme modulus, where we expect the mesenchyme is becoming stiffer due to both extracellular matrix (ECM) remodeling and muscle differentiation (27). Thus, in the second step, both the "endoderm" (now endoderm to inner longitudinal muscle) thickness and the modulus ratio increases to $\mu_e/\mu_m = 7$. Finally, in the third step, the endoderm grows again as a stiffer material (Fig. 4*C*).

The result of this simulation is a morphology strikingly similar to that of the hindgut at E14 (Figs. 4*D* and 1*D*). Along with creases, a wrinkling pattern appears at the base of the "endoderm" as it grows against outer muscle. Accordingly, the prior step at E12, which does not incorporate a change in modulus ratio and the third step of growth after remodeling, produces small wavelength creases only (Fig. 4*D*). Thus, the simultaneous presence of creases and large-scale wrinkles in the hindgut appears to depend on a change in the deforming layer geometry and elasticity as well as a critical transition where the superficial creased morphology is stabilized, which we confirmed using mechanical tissue separation.

Discussion and Conclusions

Epithelial folding has long been recognized as a critical feature underlying gut function, and though several studies have focused on morphogenesis of small intestinal villi, considerably less attention has been paid to the other segments of the gut (22, 31, 32). Furthermore, many studies have used computational and material models to understand the diverse buckled topographies found in nature, but few have incorporated systematically measured data from a developing biological system where different patterns appear within the same organ. This study uncovers the underlying mechanical mechanisms for morphological regionalization across functionally distinct segments of the gut and demonstrates that a remarkably small range and number of physiological parameters can drive formation of unique morphologies in serially homologous structures.

Trends in Geometric and Physical Parameters Appear along the Chick Gut As Morphologies Become Distinct. Modulus measurements have revealed a linear trend of decreasing modulus ratio from foregut to hindgut. Geometric parameters show modest trends during most of lumen morphogenesis (E8 to E14) as well, with radius ratio decreasing positionally from anterior to posterior, and thickness ratio generally increasing (Fig. 2 *D* and *E* and *SI Appendix*, Fig. S4*C*). Anterior–posterior gradients of biochemical signals and transcription factors are classic and fundamental tools the embryo uses to pattern the body. In the gut, multiple posterior-to-anterior gradients (with some evidence of cross-talk between them) help determine regional identity (3, 4, 33). By contrast, such large-scale mechanical trends as we note here have not received as much attention, but several recent studies have discovered gradients of mechanical properties including stiffness, fluid/solid-like properties, and contractility that guide morphogenesis on the scale of collective cell behaviors (34–36). In some of these cases, mechanical trends can be directly linked to morphogen gradients. It therefore stands to reason that this anterior–posterior pattern in physical properties along the gut may trace to a larger organizational scheme orchestrated by molecular cues.

Axial Prestretch in the Foregut is Consistent with the Maintenance of Circumferential Ridges. Several studies have reported the presence of longitudinal stretch in the esophagus at embryonic and postnatal stages, which may arise from a mismatch between the elongation rates of the foregut and other axially growing structures (37). In the mouse, longitudinal tension contributes both to the helical orientation of smooth muscle and the transition of basal epithelial progenitors from a developmental to homeostatic phenotype after birth (38, 39). Here, we report longitudinal prestretch in the chick foregut, specifically in the inner endoderm–mesenchyme composite relative to the outer muscle. It is possible that growth of the foregut tube bilayer while stretched, where the layers have different stiffnesses, would lead to the appearance and stabilization of inner composite tension relative to muscle.

Longitudinal stretch is a well-established feature of arteries that prevents circumferential deformation (40, 41). This effect is mediated by deposition of elastin, and the loss or dampening of axial tension with age leads to aberrant buckling, such as in the femoral artery (42). We expect that longitudinal prestretch prevents buckling of the foregut lumen into zigzags upon differentiation of outer and inner longitudinal smooth muscle layers. Thus, the fundamental phenomenon of axial stretch in foregut development may underlie the common morphological feature of axial, but not circumferential, buckling in the lumen.

Distinct Primary Wrinkling and Creasing Patterns along the Gut Are Tuned by a Few Physical Parameters. At E8 in the gut, isotropic growth of the endoderm can lead to either smoothly wrinkled (foregut/midgut) or cusped (hindgut) lumen morphologies due to distinct geometric and mechanical properties that help differentially shape the endoderm. The estimated initial geometries of the E8 foregut, E8 hindgut, and E10 hindgut used in simulations are listed in *SI Appendix*, Table S1. By simply incorporating these geometric and mechanical properties to the numerical models, we could obtain distinct wrinkles and creases as shown in Fig. 3*B* (Movies S1 and S2) and Fig. 4*A* (Movies S4 and S5). For the stiff and thin endoderm model replicating the foregut ($\mu_e/\mu_m = 35$ and $h_e/h_m = 0.3$), the primary buckling is sinusoidal wrinkling; for a softer and thicker endoderm model as in the hindgut ($\mu_e/\mu_m = 2$ and $h_e/h_m = 0.5$), the primary buckling is creasing, which is not initialized from sinusoidal

Downloaded from https://www.pnas.org by "HARVARD UNIVERSITY, CABOT SCIENCE LIBRARY" on August 11, 2024 from IP address 140.247.148.200.

wrinkling. Then, anisotropic growth of the foregut endoderm progresses primary buckling in the foregut to self-contacting folding.

Clearly, only a slight change in elastic and geometric parameters can sufficiently explain the initial divergence in primary lumen surface patterns along the gut. We note, however, that our approach does not predict the exact quantitative properties of a given lumen pattern, such as wave number and length, but is rather able to capture key shape differences across compartments and trends in pattern evolution over developmental time. A fine-grained computational exploration of the parameter space defined by geometry, stiffness, and growth could lend insight into individual variations in morphology, which are collapsed into average values in this study.

Ideally, such a computational approach would be complemented by a concomitant experimental exploration of the parameter space, which would serve as an independent test of the model. Conventional methods in the chick, such as genetic or pharmacological perturbations, often do not address a single parameter in isolation due to simultaneous effects on multiple properties of interest, like thickness and stiffness. However, much like the silk tubes used to constrain midgut inner layer growth in ref. 22, methods combining inert synthetic and biological materials may be useful in overcoming current experimental limitations. For example, deformable polydimethylsiloxane (PDMS) substrates carefully designed to have varying thicknesses and stiffnesses could be leveraged as substrates for ex vivo culture of tissue layers isolated from the gut. With the appropriate growth conditions, the resulting buckling instabilities could be mapped back to the hypothetical parameter space generated from model simulations.

Importantly, our focus in this study was on the tubular regions of the intestine and esophagus, and not on components with more complex geometries such as the stomach, ceca, crop, or cloaca, for reasons outlined above. Thus, though current iterations of the computational model could easily be generalized to other growing, multilayer biological tubes in developmental or pathogenic contexts (e.g., arteries), modeling gut regions with varied macroscopic morphologies would require modifications to the geometric framework. For example, studies of crop or stomach morphogenesis could approximate the computational domain as a 3D spherical shell, with corresponding changes to the design of the 3D spatiotemporal anisotropic growth tensor field. Because the lumens of these gut regions also develop morphologies like ridges and irregular zigzags, we expect the same general principles established in this study to apply to lumen morphogenesis in nontubular structures derived from the primordial gut tube. Future studies will be needed to support this expectation.

Postbuckling Period-Doubling in the Foregut Due to Anisotropic Growth. Period-doubling has long been observed and investigated in many film-substrate systems (43, 44). However, only two types of the period-doubling have been reported and simulated under the assumption of global compression or isotropic film growth. Here, we explore period-doubling in the context of foregut tube morphogenesis, and present three cases with varying geometric, growth, and modulus parameters (Fig. 3 *D*, *I*, *II*, and *III* and Movie S3). Of these, we find that endodermal thinning in the context of a high endoderm-to-mesenchyme modulus ratio agrees with the secondary postbuckling pattern of chick foregut at E17. Relative thinning of the endoderm, in fact, is a key temporal parameter in all foregut simulations. Interestingly, the esophageal mucosa thins as it matures from a pseudostratified cuboidal to a stratified squamous epithelium (45). Therefore, the processes that lead to cytological differentiation of the epithelial layer may also contribute to the extensive elaboration of its folding pattern.

Bifurcated folds are highly conserved morphological features of the mature esophagus. In contrast to arrays of adjacent villi in the small intestine with roughly equal heights and widths, the esophagi of snakes, chickens, humans, and other mammals show doubled or secondary folds (46–48). While the functional relevance of these morphologies is unclear, it is worth noting that the progressive doubling of axial folds eventually coincides with the formation of longitudinally aligned secretory gland invaginations, suggesting that perhaps bifurcations are relevant to the patterning of gland positions along the mucosal surface (9).

Multiscale Surface Creasing and Interfacial Folding in Hindgut. During the late stages of hindgut development, the lumen progressively grows and the endoderm continues thinning, resulting in primary creases adopting smaller wavelengths. Fig. 4*B* shows that the surface creasing pattern is maintained even if the endoderm–mesenchyme composite is dissected from the muscle layer at E12. This indicates a possible tissue remodeling process during which the endoderm releases the residual stresses induced by incompatible growth. We therefore invoked a stepwise growing process, during which endoderm isotropic growth is followed by stress-releasing remodeling (Fig. 4*C*). Then, an increase in both effective endoderm thickness and modulus ratio when considering the intermediate muscle layer as part of stiffer inner longitudinal layer leads to a secondary multiscale creasing-wrinkling pattern at E14. Importantly, the primary small-wavelength surface creasing pattern is maintained (Fig. 4*D* and Movies S6 and S7).

One explanation for the persistence of creases upon dissection is that stiffening and thickening induced by the remodeling of subepithelial ECM in the hindgut leads to constraint of the endoderm predominantly by the mesenchyme rather than the muscle (27). One way future studies could investigate this further would be to incorporate ECM remodeling into the computational framework: Our current model is a quasi-static elastic model with a plastic growing part. The long-timescale relaxation and remodeling process is achieved through a stress-releasing step. Remodeling of ECM can be more precisely described by a viscoelastic model, which captures the dynamic stress-relaxation with a characteristic viscous timescale. These parameters could be measured through, for example, a creep test, which would reveal the viscoelastic properties of the tissues over the course of hindgut lumen buckling into primary and secondary forms.

As with period-doubling, the functional consequence of secondary multiscale wrinkling in the hindgut is not clear. However, these folds are at least superficially analogous to anal columns, or columns of Morgagni, which are broad axial folds that form at the very posterior end of the rectum (49). The positional patterning gene Hoxd13 regulates formation of smooth muscle in the caudal intestine, and leads to anal sphincter defects when mutated (50). When this gene is misexpressed in the chick midgut, hindgut multiscale folding and inner longitudinal layer differentiation is replicated, suggesting a possible conserved role for these folds in proper functioning of the rectum (27).

Materials and Methods

Section Immunostaining. Tissues were fixed for 2 h at room temperature in 4% paraformaldehyde (PFA) in 1X Phosphate-Buffered Saline (PBS); they were then washed, dehydrated in 3% sucrose in 1X PBS and embedded in

Downloaded from https://www.pnas.org by "HARVARD UNIVERSITY, CABOT SCIENCE LIBRARY" on August 11, 2024 from IP address 140.247.148.200.

cryomolds containing Tissue-Tek O.C.T. Compound. Samples were kept as tubes for transverse section images, and cut open and pinned flat prior to fixation for sagittal sections. Guts were sectioned onto Superfrost slides as 16 μm thick slices and allowed to dry before being permeabilized with PBSTT (1X PBS + 0.1% Tween-20 + 0.05% Triton-X100). The following primary antibodies were then applied at 4 °C overnight: SMA-FITC (1:1,000, F3777 Sigma), calponin 1 (1:100, Cell Signaling). A donkey anti-rabbit Alexa647 secondary antibody (Jackson Immuno) was used for calponin stains at a 1:300 dilution in PBSTT at room temperature for 2 h. Stained sections were imaged on a compound epifluorescence microscope.

Fold Morphology Measurements. Geometric properties of foregut and midgut wrinkles were measured in ImageJ from transverse DAPI (4′,6-diamidino-2-phenylindole)-stained sections, or from depth-coded projections of lumen surfaces. For wrinkle number and aspect ratio, sections were imaged on a compound epifluorescence microscope. The number of wrinkles per cross-section was counted for each full section, and wrinkle aspect ratios and wavelengths were measured using the line segment tool. Aspect ratios were measured as described in ref. 27 from randomly sampled wrinkles taken from three transverse sections per region and time points. Wrinkle wavelengths were measured from the center points of adjacent longitudinal folds on the circumferential axis.

Lumen Surface Imaging. Surfaces of intestinal segments were imaged by longitudinally slicing and pinning gut tubes flat for 2 h at room temperature in 4% PFA (27). DAPI-stained, fixed guts were imaged on a Zeiss LSM 710 point-scanning inverted confocal microscope. Depth coding was performed using the Temporal Color Code function in ImageJ.

Whole Mount Immunostaining and Tissue Clearing. Tissue clearing was performed for fixed whole guts older than E12. Samples to be immunostained were dehydrated through a methanol series (1 h incubations in 20, 40, 60, 80, 100, and 100% methanol in distilled water), followed by rehydration the same way in methanol + 1X PBS. Guts were then permeabilized in 1X PBS containing 0.1% Triton-X100 and 1% BSA for 4 to 6 h, and incubated in SMA-FITC (1:300, F3777 Sigma) at 4 °C for 3 to 5 d. Following 2 d of washes in the permeabilization solution, guts were postfixed for 2 h at room temperature in 4% PFA, followed by washes and dehydration through a methanol series as before. Two 1-h incubations with dichloromethane were performed after transferring tissues to 5 mL glass vials, followed by a 1-h incubation in ethyl cinnamate. Stained, cleared tissues were imaged in ethyl cinnamate, in the same fashion as lumen surface imaging described above.

Muscle Orientation Analysis. SMA-stained whole guts were imaged in the same way as DAPI-stained lumen surfaces described above. Maximum projections encompassing each muscle layer were divided into 100 μm × 100 μm sample images, and the OrientationJ plugin in ImageJ was used to determine the distribution of fiber angles present in each image. Results returned in 180° were limited to a 0 to 90° axis by adding −90 to 0 and 0 to 90 distributions.

Differential Growth Measurements. Whole guts were dissected and cut into 250 μm thick rings (circumferential) or 1 to 2 mm segments (longitudinal) using a vibratome (Fig. 2*I*). Samples were transferred to a 3% agarose dish with 1X PBS and predissection images were taken using a Leica stereoscope camera. Inner layers were carefully dissected from outer muscle using electrolytically sharped, 0.002-in-diameter tungsten needles. Dissected tissues were allowed to relax for 30 min before postdissection images were taken. Strain was calculated as the percent change in inner composite length upon compression into the stressed configuration [(predissection length-postdissection length)/predissection length] (Fig. 2*I*). Radii and tissue layer thicknesses over time were measured as shown in Fig. 2*A* using DAPI and SMA-stained transverse sections.

Modulus Measurements. Dissected tissue rings were first immobilized using a tungsten rod pierced through the lumen (without puncturing the tissue) and into a 3% agarose dish filled with PBS. A tungsten cantilever connected to a motorized actuator was hooked into the lumen, which was then programmed to stretch the tissue at a constant velocity of 0.002 mm/s using custom software (Fig. 2*F*). Timelapse movies were analyzed in MATLAB. Strain was calculated from the percent change in distance between dots over time, and stress was calculated as $\sigma = k_b\delta/2\,\mathrm{wl}$, where δ is the deflection of the tungsten cantilever, and 2 wl is the cross-sectional area of the tissue ring. k_b is the bending stiffness of the cantilever, defined as $k_b = 3EI/L^3$. E is Young's modulus of tungsten, L is the length of the lever, and I is the area moment of inertia of a circle, or $I = \pi(r^4)/4$, where r is the radius of the lever (Fig. 2*F*). Young's modulus was determined from the slope of the resulting stress–strain curve in the small strains regime, corresponding to actual measured strains. Mesenchyme modulus was determined from endoderm and composite moduli and thicknesses, as shown in *SI Appendix*, Fig. S4*A*. SE for mesenchyme modulus and modulus ratio was propagated from thickness and modulus measurement errors.

Finite Element Method. We used the finite element method to track primary and secondary bifurcation patterns. We assumed both isotropic and anisotropic growth of endoderm and mesenchyme layers using user-defined material subroutines (UMAT/VUMAT) implemented in commercial software Abaqus/Standard (6.14). The geometric and physical parameters are shown in *SI Appendix*, Table S1. For each model, convergency is ensured using tests with finer meshgrids.

Data, Materials, and Software Availability. Microscopy data used for experimental measurements and scripts used for computational simulations are publicly available via Zenodo (51, 52). All other data are included in the article and/or supporting information.

ACKNOWLEDGMENTS. We acknowledge financial support from NSF-ANR (French National Research Agency) grant 2204058 (S.Y. and L.M.), NIH grant (L.M.), the Simons Foundation (L.M.), the Henri Seydoux Fund (L.M.), and NIH Award 5RO1HD087234 (C.J.T.). Portions of this paper were developed from the thesis of H.K.G.

Author affiliations: [a]Department of Genetics, Blavatnik Institute, Harvard Medical School, Boston, MA 02115; [b]Harvard John A. Paulson School of Engineering and Applied Sciences, Harvard University, Cambridge, MA 02138; [c]Department of Pharmaceutical Chemistry, University of California, San Francisco, CA 94158; [d]The Fu Foundation School of Engineering and Applied Science, Department of Biomedical Engineering, Columbia University, New York, NY 10027; [e]Department of Physics, Harvard University, Cambridge, MA 02138; and [f]Department of Organismic and Evolutionary Biology, Harvard University, Cambridge, MA 02138

1. V. Hartenstein, P. Martinez, Structure, development and evolution of the digestive system. *Cell Tissue Res.* **377**, 289–292 (2019).
2. J. R. Spence, R. Lauf, N. F. Shroyer, Vertebrate intestinal endoderm development. *Dev. Dyn.* **240**, 501–520 (2011).
3. D. J. Roberts *et al*., Sonic hedgehog is an endodermal signal inducing Bmp-4 and Hox genes during induction and regionalization of the chick hindgut. *Development* **121**, 3163–3174 (1995).
4. R. I. Sherwood, R. Maehr, E. O. Mazzoni, D. A. Melton, Wnt signaling specifies and patterns intestinal endoderm. *Mech. Dev.* **128**, 387–400 (2011).
5. L. W. Peterson, D. Artis, Intestinal epithelial cells: Regulators of barrier function and immune homeostasis. *Nat. Rev. Immunol.* **14**, 141–153 (2014).
6. D. Ménard, Morphological studies of the developing human esophageal epithelium. *Microsc. Res. Tech.* **31**, 215–225 (1995).
7. D. B. Wake, *Biology of the Reptilia* (Morphology e, 1978), vol. 6.
8. D. Liao, J. Zhao, J. Yang, H. Gregersen, The oesophageal zero-stress state and mucosal folding from a GIOME perspective. *World J. Gastroenterol* **13**, 1347 (2007).
9. S. A. Soliman, F. A. Madkour, Developmental events and cellular changes occurred during esophageal development of quail embryos. *Sci. Rep.* **11**, 7257 (2021).
10. V. K. Gohel, S. L. Edell, I. Laufer, W. H. Rhodes, Transverse folds in the human esophagus. *Radiology* **128**, 303–308 (1978).
11. M. S. Levine, S. E. Rubesin, Diseases of the esophagus: Diagnosis with esophagography. *Radiology* **237**, 414–427 (2005).
12. Y. Zhang, D. Bailey, P. Yang, E. Kim, J. Que, The development and stem cells of the esophagus. *Development* **148**, dev193839 (2021).
13. V. Bonis, C. Rossell, H. Gehart, The intestinal epithelium-fluid fate and rigid structure from crypt bottom to villus tip. *Front. Cell Dev. Biol.* **9**, 661931 (2021).

Downloaded from https://www.pnas.org by "HARVARD UNIVERSITY, CABOT SCIENCE LIBRARY" on August 11, 2024 from IP address 140.247.148.200.

14. H. Gehart, H. Clevers, Tales from the crypt: New insights into intestinal stem cells. *Nat. Rev. Gastroenterol. Hepatol.* **16**, 19–34 (2019).
15. P. de Santa, G. R. Barbara, V. Den Brink, D. J. Roberts, Development and differentiation of the intestinal epithelium. *Cell. Mol. Life Sci.* **60**, 1322–1332 (2003).
16. A. Kostouros *et al*., Large intestine embryogenesis: Molecular pathways and related disorders. *Int. J. Mol. Med.* **46**, 27–57 (2020).
17. C. A. Rubio, Innominate grooves of the colon: Histological reappraisal. *Anticancer Res.* **40**, 7031–7035 (2020).
18. L. Bell, L. Williams, A scanning and transmission electron microscopical study of the morphogenesis of human colonic villi. *Anat. Embryol.* **165**, 437–455 (1982).
19. Z. X. Mahoney, T. S. Stappenbeck, J. H. Miner, Laminin *alpha*5 influences the architecture of the mouse small intestine mucosa. *J. Cell Sci.* **121**, 2493–2502 (2008).
20. G. M. H. Birchenough, E. E. L. Nyström, M. E. V. Johansson, G. C. Hansson, A sentinel goblet cell guards the colonic crypt by triggering Nlrp6-dependent Muc2 secretion. *Science* **352**, 1535–1542 (2016).
21. K. Parikh *et al*., Colonic epithelial cell diversity in health and inflammatory bowel disease. *Nature* **567**, 49–55 (2019).
22. A. E. Shyer *et al*., Villification: How the gut gets its villi. *Science* **342**, 212–218 (2013).
23. C. M. Nelson, On buckling morphogenesis. *J. Biomech. Eng.* **138**, 021005 (2016).
24. L. Wang, C. E. Castro, M. C. Boyce, Growth strain-induced wrinkled membrane morphology of white blood cells. *Soft Matter* **7**, 11319–11324 (2011).
25. T. Tallinen, J. S. Biggins, Mechanics of invagination and folding: Hybridized instabilities when one soft tissue grows on another. *Phys. Rev. E* **92**, 022720 (2015).
26. Q. Wang, X. Zhao, A three-dimensional phase diagram of growth-induced surface instabilities. *Sci. Rep.* **5**, 8887 (2015).
27. H. K. Gill *et al*., Hox genes modulate physical forces to differentially shape small and large intestinal epithelia. bioRxiv [Preprint] (2023). https://dx.doi.org/10.1101/2023.03.15.532602 (Accessed 20 June 2023).
28. Nandan L. Nerurkar, Lakshminarayanan Mahadevan, Clifford J. Tabin, Bmp signaling controls buckling forces to modulate looping morphogenesis of the gut. *Proc. Natl. Acad. Sci. U.S.A.* **114**, 2277–2282 (2017).
29. R. R. Shah, N. L. Nerurkar, C. C. Wang, J. L. Galloway, Tensile properties of craniofacial tendons in the mature and aged zebrafish. *J. Orthop. Res.* **33**, 867–873 (2015).
30. T. Tallinen, J. S. Biggins, L. Mahadevan, Surface sulci in squeezed soft solids. *Phys. Rev. Lett.* **110**, 024302 (2013).
31. A. M. Freddo *et al*., Coordination of signaling and tissue mechanics during morphogenesis of murine intestinal villi: A role for mitotic cell rounding. *Integr. Biol.* **8**, 918–928 (2016).
32. K. D. Walton, Villification in the mouse: Bmp signals control intestinal villus patterning. *Development* **143**, 427–436 (2016).
33. L. Raghoebir *et al*., Sox2 redirects the developmental fate of the intestinal epithelium toward a premature gastric phenotype. *J. Mol. Cell Biol.* **4**, 377–385 (2012).
34. H. J. Gustafson, N. Claussen, S. De Renzis, S. J. Streichan, Patterned mechanical feedback establishes a global myosin gradient. *Nat. Commun.* **13**, 7050 (2022).
35. N. L. Nerurkar, C. H. Lee, L. Mahadevan, C. J. Tabin, Molecular control of macroscopic forces drives formation of the vertebrate hindgut. *Nature* **565**, 480–484 (2019).
36. D. Pinheiro, R. Kardos, É. Hannezo, C.-P. Heisenberg, Morphogen gradient orchestrates pattern-preserving tissue morphogenesis via motility-driven unjamming. *Nat. Phys.* **18**, pages1482–1493 (2022).
37. S. R. Fausett, J. Klingensmith, Compartmentalization of the foregut tube: Developmental origins of the trachea and esophagus. *Wiley Interdiscip. Rev. Dev. Biol.* **1**, 184–202 (2012).
38. T. R. Huycke *et al*., Genetic and mechanical regulation of intestinal smooth muscle development. *Cell* **179**, 90–105 (2019).
39. J. McGinn *et al*., A biomechanical switch regulates the transition towards homeostasis in oesophageal epithelium. *Nat. Cell Biol.* **23**, 511–525 (2021).
40. C.-J. Chuong, Y.-C. Fung, "Residual stress in arteries" in *Frontiers in Biomechanics*, G. W. Schmid-Schonbein, S. L. Y. Woo, B. W. Zweifach, Eds. (Springer, New York, NY, 1986), pp. 117–129.
41. L. Hornỳ, M. Netušil, T. Voňavková, Axial prestretch and circumferential distensibility in biomechanics of abdominal aorta. *Biomech. Model. Mechanobiol.* **13**, 783–799 (2014).
42. A. V. Kamenskiy *et al*., Passive biaxial mechanical properties and in vivo axial pre-stretch of the diseased human femoropopliteal and tibial arteries. *Acta Biomater.* **10**, 1301–1313 (2014).
43. K. Efimenko *et al*., Nested self-similar wrinkling patterns in skins. *Nat. Mater.* **4**, 293–297 (2005).
44. B. Li, Y.-P. Cao, X.-Q. Feng, H. Gao, Surface wrinkling of mucosa induced by volumetric growth: Theory, simulation and experiment. *J. Mech. Phys. Solids* **59**, 758–774 (2011).
45. Y. Zhang, D. Bailey, P. Yang, E. Kim, J. Que, The development and stem cells of the esophagus. *Development* **148**, 03 (2021).
46. W. Khamas, R. Reeves, Morphological study of the oesophagus and stomach of the gopher snake pituophis catenifer. *Anat. Histol. Embryol.* **40**, 307–313 (2011).
47. K. Martyniuk, N. Ziółkowska, M. Hanuszewska-Dominiak, N. Szyryńska, B. Lewczuk, Histology and ultrastructure of the esophagus in European beaver (castor fiber) displays features adapted to seasonal changes in diet. *Animals* **13**, 635 (2023).
48. W. M. Weinstein, E. R. Bogoch, K. L. Bowes, The normal human esophageal mucosa: A histological reappraisal. *Gastroenterology* **68**, 40–44 (1975).
49. C. M. Goss, Gray's anatomy of the human body. *Acad. Med.* **35**, 90 (1960).
50. T. Kondo, P. Dollé, J. Zákány, D. Duboule, Function of posterior HoxD genes in the morphogenesis of the anal sphincter. *Development* **122**, 2651–2659 (1996).
51. H. Gill, Experimental Data for "the Developmental Mechanics of Divergent Buckling Patterns in the Chick Gut". Zenodo. https://dx.doi.org/10.5281/zenodo.11660711. Deposited 14 June 2024.
52. S. Yin, Numerical Simulation Codes for "the Developmental Mechanics of Divergent Buckling Patterns in the Chick Gut". Zenodo. https://dx.doi.org/10.5281/zenodo.11995760. Deposited 17 June 2024.

Downloaded from https://www.pnas.org by "HARVARD UNIVERSITY, CABOT SCIENCE LIBRARY" on August 11, 2024 from IP address 140.247.148.200.